Surface & Coatings Technology 468 (2023) 129733

Contents lists available at ScienceDirect

Surface & Coatings Technology

journal homepage: www.elsevier.com/locate/surfcoat

High-temperature oxidation resistance of ternary and quaternary Cr-(Mo)-Si-B_{2-z} coatings — Influence of Mo addition

A. Bahr [a,*], T. Glechner [a], A. Grimmer [a], T. Wojcik [a], R. Hahn [a], P. Kutrowatz [a], M. Podsednik [b], A. Limbeck [b], M. Heller [c], J. Ramm [d], O. Hunold [d], S. Kolozsvári [e], P. Polcik [e], E. Ntemou [f], D. Primetzhofer [f], P. Felfer [c], H. Riedl [a,g]

[a] Christian Doppler Laboratory for Surface Engineering of high-performance Components, TU Wien, A-1060 Wien, Austria
[b] Institute of Chemical Technologies and Analytics, TU Wien, A-1060 Wien, Austria
[c] Department of Materials Science, Friedrich-Alexander-Universität Erlangen-Nürnberg, D-91058 Erlangen, Germany
[d] Oerlikon Balzers, Oerlikon Surface Solutions AG, LI-9496 Balzers, Liechtenstein
[e] Plansee Composite Materials GmbH, D-86983 Lechbruck am See, Germany
[f] Department of Physics and Astronomy, Uppsala University, SE-75120 Uppsala, Sweden
[g] Institute of Materials Science and Technology, TU Wien, A-1060 Wien, Austria

ARTICLE INFO

Keywords:
Chromium diboride
Disilicides
Sputtering
Thin films
Oxidation resistance

ABSTRACT

The Si-based alloying of transition metal diborides is a promising strategy to improve their limited oxidation resistance in high-temperature environments. In this study, we investigate the oxidation resistance of ternary and quaternary Cr-(Mo)-Si-B_{2-z} coatings sputter-deposited from alloyed CrB_2/$TMSi_2$ targets (TM = Cr or Mo). The as-deposited Cr-(Mo)-Si-B_{2-z} coatings are stabilized in the single-phased hexagonal AlB_2-structure, except the high-Si containing $Cr_{0.26}Mo_{0.11}Si_{0.24}B_{0.39}$ presenting amorphous character. The Mo-containing Cr-Mo-Si-B_{2-z} films exhibit relatively high hardness compared to their ternary Cr-Si-B_{2-z} counterparts, obtaining up to 26 GPa due to the formation of (Cr,Mo)B_2 solid solutions. The Si-alloying in ternary and quaternary coatings provides oxidation resistance up to 1200 °C, owing to the formation of highly protective double-layered scales consisting of SiO_2 with a Cr_2O_3 layer on top, inhibiting oxygen inward diffusion. The quaternary $Cr_{0.31}Mo_{0.07}Si_{0.15}B_{0.47}$ coating is distinguished by superior oxidation resistance with lower porosity and void formation compared to the ternary $Cr_{0.37}Si_{0.16}B_{0.47}$. Mo proved to be the key element for the higher stability and enhanced oxidation resistance due to the evolution of the $MoSi_2$ phase at ~600 °C. This phase formation controls the Si diffusion and mobility within the microstructure, thus reducing the porosity and governing the Si supply to form SiO_2 scale. The quaternary $Cr_{0.31}Mo_{0.07}Si_{0.15}B_{0.47}$ coating maintained an oxidation resistance up to 30 h at 1200 °C by forming a 2.5 μm dense amorphous Si-based oxide scale with a thin Cr_2O_3 on top.

1. Introduction

The performance and efficiency of components operating in high-temperature applications (e.g. jet turbine engines) are primarily dependent on the operating temperature limits set by the bulk material [1]. By applying surface protective coatings, efficiency and performance can be improved by pushing the operating temperatures of components beyond their substrate material service temperature limits. Hence, this requires the development of novel coating materials with a refractory character and the highest stability at elevated temperatures (e.g. > 1200 °C). Transition metal diborides (TMB_2) represent a highly interesting and promising group of materials to be applied as the next generation of protective coatings in various high-temperature applications due to their refractory properties of high melting points, hardness, and excellent chemical stability [2–4]. However, a major limitation of TMB_2 materials is their poor oxidation resistance at high temperatures [5–8], besides low fracture toughness due to inherent brittleness [9–11].

The oxidation behavior of the well-known group IV transition metal diborides (TiB_2, ZrB_2, and HfB_2) have been extensively studied as bulk materials. These bulk TMB_2 systems tend to form mixed oxide scales of TMO_2 and B_2O_3 at around 400 °C. In the high-temperature regime (>1000 °C), the formed oxide scales are non-protective due to the

* Corresponding author.
E-mail address: ahmed.bahr@tuwien.ac.at (A. Bahr).

https://doi.org/10.1016/j.surfcoat.2023.129733
Received 13 May 2023; Received in revised form 13 June 2023; Accepted 17 June 2023
Available online 21 June 2023

evaporation of B_2O_3 and the formation of porous TMO_2 scales [5,6,12]. As coating materials, binary $TMB_{2\pm z}$ films exhibit inferior oxidation behavior compared to their bulk counterparts due to the rapid evaporation of B_2O_3 at lower temperatures (< 800 °C) accompanied by the formation of porous TMO_2-based scales. The absence of glassy B_2O_3 at intermediate temperatures is a limiting factor for $TMB_{2\pm z}$ based coatings [7,13–16]. The poor oxidation resistance of binary $TMB_{2\pm z}$ coatings stimulated studies on the development of alloying strategies to design novel ternary transition metal diborides (TM-X-$B_{2\pm z}$) with enhanced high-temperature oxidation resistance. So far, several attempts have been carried out to enhance the oxidation resistance of $TMB_{2\pm z}$ films based on alloying with elements that are capable of forming protective oxide scale at high temperatures such as Al [8,17], Ta [16], and Si [15,18–20]. Compared to other alloying routes, the Si alloying of $TMB_{2\pm z}$ provides superior oxidation resistance, especially in the high-temperature regime (> 1000 °C), due to the formation of highly protective Si-based scales [15]. Glechner et al. reported strongly retarded oxidation kinetics above 1100 °C for ternary Ti-Si-$B_{2\pm z}$, Hf-Si-$B_{2\pm z}$, and Cr-Si-$B_{2\pm z}$ coatings [15,18,21]. Nevertheless, the Cr-Si-$B_{2\pm z}$ coatings exhibit the highest oxidation resistance among all reported systems with very low oxide growth rates up to 1200 °C based on the formation of layered, protective scales mainly consisting of amorphous sub-layer SiO_2 with Cr_2O_3 on top [15]. Moreover, Glechner et al. reported that the amount of boron plays also a decisive role - besides the Si content - in the oxidation behavior of Cr-Si-$B_{2\pm z}$, where accelerated scale growth kinetics were observed for the higher boron containing $Cr_{0.27}Si_{0.09}B_{0.64}$ compared to $Cr_{0.26}Si_{0.16}B_{0.58}$ [21]. Zauner et al. recently indicated the solubility limit of Si in the AlB_2-structured Cr-Si-$B_{2\pm z}$ to be around 4 at. %, where excess Si tends to segregate towards grain boundaries. Moreover, an optimum Si-content of ~8 at. % is required to improve the oxidation resistance of Cr-Si-$B_{2\pm z}$ coatings [20]. The reported high-temperature oxidation resistance is attributed to the formation of protective Si-based scales. However, the outward diffusion of excess Si towards the surface leaves a high degree of porosity within the coating [20]. Additionally, high Si contents decrease the hardness of Cr-Si-$B_{2\pm z}$ coatings compared to binary $CrB_{2\pm z}$ [15,20].

A successful strategy to improve the oxidation resistance of bulk TMB_2 systems (especially for ZrB_2 and HfB_2) is the alloying with secondary Si-based phases of SiC or $TMSi_2$ [22–25]. Among different Si-based phases, $MoSi_2$ receives considerable research interest due to its outstanding oxidation resistance in high-temperature regimes within bulk and thin film materials [26,27]. Silvestroni et al. explored the alloying of bulk ZrB_2 with various $TMSi_2$ (TM = Zr, Mo, Ta and W), and reported the $MoSi_2$ to be the best additive for improving the oxidation resistance of ZrB_2 in the temperature range between 1200 and 1800 °C, due to formation of Si-rich scale and subsurface refractory phases of MoB and Mo_5Si_3 [23,28]. Furthermore, the Mo-alloying is reported to enhance the mechanical properties of Cr-based systems (e.g. Cr—Si) in terms of fracture toughness and creep resistance [29,30].

The alloying based on $TMSi_2$ is a promising strategy to be applied for TMB_2 thin film coating materials to enhance the oxidation resistance without the deterioration of mechanical properties. For TiB_2 coatings, the $TMSi_2$ alloying was recently proven to be a successful strategy yielding quaternary diboride coatings with remarkable high-temperature oxidation resistance and good mechanical stability [31].

In the present study, we investigate the high-temperature oxidation resistance of novel quaternary Cr-Mo-Si-B_{2-z} in comparison with ternary Cr-Si-B_{2-z} and binary CrB_{2-z} coating materials. The coatings are deposited by DC magnetron sputtering from alloyed $CrB_2/TMSi_2$ target materials with various compositions. The main focus is to study the influence of Mo and Si on the phase formation, hardness and oxidation behavior of the alloyed coatings.

2. Experimental details

All the coatings were synthesized in a laboratory-scale magnetron sputtering system using 3-in. sized CrB_2-based targets alloyed with $TMSi_2$ secondary phases (Plansee Composite Materials GmbH). The employed targets are $CrB_2/CrSi_2$ (90/10 and 80/20 mol%) as well as $CrB_2/MoSi_2$ (90/10, 80/20, and 70/30 mol%). The depositions were carried out in a pure argon atmosphere (working pressure of 0.4 Pa) by sputtering each of the mentioned targets solely in a DC mode at 0.4 A (200 W). The base pressure before all depositions was maintained below 10^{-4} Pa. Additionally, a binary $CrB_{1.5}$ coating was grown from a pure CrB_2 target at a working pressure of 0.56 Pa. For all depositions, the substrate temperature was maintained at 550 °C, whereas the rotating substrate holder (0.25 Hz) was mounted parallel to the target at a distance of 90 mm. Furthermore, a substrate DC bias potential was applied between −40 V and − 150 V. The coatings were deposited on single crystalline Si (100-oriented, 20x7x0.38 mm^3), single crystalline sapphire ($10\bar{1}1$-oriented, 10x10x0.53 mm^3), and poly-crystalline Al_2O_3 (20x7x0.38 mm^3) substrates. Prior to the depositions, the bare substrates were cleaned in an ultrasonic bath using acetone and ethanol. Afterwards, a plasma cleaning step of the substrates is carried out for 10 min in pure Ar at 5 Pa.

The chemical composition of the coatings was determined by ion beam analysis techniques using Time-of-Flight Elastic Recoil Detection Analysis (ToF-ERDA) and Rutherford Backscattering Spectrometry (RBS) at the 5 MV Pelletron Tandem accelerator laboratory at Uppsala University [32]. For ToF-ERDA, $^{127}I^{8+}$ projectiles with a primary energy of 36 MeV were employed with an incident angle of 67.5° with respect to the surface normal while recoils were detected at an angle of 45° with respect to the incident beam. RBS was carried out using 3 MeV $^4He^+$ ions and a detection angle of 170°. The analysis of the ToF-ERDA experimental data was performed using the Contes software [33], while the RBS data were analyzed using the SIMNRA software [34,35]. The RBS-analysis provides primarily information on the concentration ratio of transition metals as well as confirms constant concentrations over a large depth range (> 1 μm), whereas ToF-ERDA provides accurate information on light species such as boron and can confirm the absence of contaminations. In combination, high accuracy without the need for reference samples can be achieved [36]. The total systematic and statistical uncertainties were estimated to be at most 5–8 % of the deduced value for the major constituents and below 15 % for the oxygen traces. Systematic uncertainties originate from plural scattering of heavy constituents (e.g. Mo) [37] and from the specific energy loss of primary ions and recoils, which is commonly known only with an accuracy of ~5 % [38]. The statistical uncertainties originate from counting statistics (1 %). Furthermore, complimentary chemical analyses were done using liquid inductively coupled plasma optical emission spectroscopy (ICP-OES). The coatings on Al_2O_3 substrates were acid digested in 0.5 mL HNO_3 and 0.5 ml HF in falcon tubes for 10 min without heating. The analyses were carried out with an iCAP 6500 RAD (Thermo Fisher, USA), with an ASX-520 autosampler (CETAC Technologies, USA) using an HF resistant sample introduction kit consisting of a Miramist nebulizer (Burger Research, USA), an alumina injector tube and a PTFE spray chamber. For each investigated element at least two non-interfered emission lines with sufficient sensitivity were selected, further instrumental parameters were used as recommended by the manufacturer. Background corrected emission signals were quantified using matrix-adjusted external calibration standards. The used method was validated in [15,39,40].

The growth morphology of the as-deposited coatings was investigated using scanning electron microscopy (SEM, Zeiss Sigma 500VP). The crystal structure was investigated by X-ray diffraction (XRD) in Bragg-Brentano configuration using a Panalytical Xpert Pro MPD system equipped with Cu-K_α radiation source (wavelength $\lambda = 1.54$ Å, operated at 45 kV and 40 mA). In order to track the phase evolution of selected coatings at elevated temperatures, in-situ XRD measurements were carried out in Bragg-Brentano configuration using an Anton Paar high-temperature furnace chamber (HTK 1200 N). The XRD measurements

were performed in vacuum at room temperature and between 500 °C and 1100 °C every 50 °C step.

The oxidation behavior of the coatings was investigated using a thermogravimetric analyzer (TGA) (Netzsch STA 449 F1) equipped with a Rhodium furnace. The dynamic measurements were carried out up to 1400 °C with a heating rate of 10 °C/min, under a flowing stream of synthetic air (50 ml/min) and helium (20 ml/min). For these experiments coated Al_2O_3 substrates (pre-weighted before deposition) have been used. For selected coatings, further isothermal annealing tests were done using a conventional furnace in ambient air at 1200 °C up to 30 h.

To investigate the morphology of the partially oxidized coatings, cross sections were prepared using a FIB-SEM dual-beam system (ThermoFisher Scientific Scios 2). The cross sections were milled using Ga^+ ion beam currents of 7–15 nA for rough milling and 1 nA for fine milling at an acceleration voltage of 30 kV. Moreover, the growth morphology for selected oxidized samples was further investigated by transmission electron microscopy (TEM, FEI TECNAI F20, equipped with a field emission gun and operated at 200 kV acceleration voltage). Additionally, energy dispersive X-ray spectroscopy (EDX) and electron energy-loss spectroscopy (EELS) mappings, as well as line scans of the partially oxidized coatings, have been conducted.

The three-dimensional distribution of elements was investigated by atom probe tomography (APT) for a selected Cr-Mo-Si-B_{2-z} coating in as-deposited and annealed states. The APT samples were prepared using a focused ion beam (FIB) (Scios 2 DualBeam system, ThermoFisher Scientific). Lift-outs were extracted from the film surfaces using ion beam currents of 3–5 nA for rough milling and 1 nA for fine milling. The acceleration voltage was set to 30 kV. Moreover, the final sharpening of the tips was performed at 50 pA, with a subsequent clean-up step at 28 pA and 5 kV. The APT analysis was done using a Cameca LEAP 4000× HR equipped with a 355 nm UV laser and a reflectron lens. The measurements were done in a pulsed laser mode employing a laser pulse energy of 50–70 pJ. The specimen temperature was at 45 K, the target evaporation rate was 1 % and the pulse rate was set to 200 kHz. Data analysis was done using a Matlab tool-box [41].

The hardness and *E*-modulus of the coatings was investigated using an ultra-micro indentation (UMIS) system equipped with Berkovich diamond tip. For each sample, 31 indents were done in a load-controlled mode with indentation loads varied between 3 and 45 mN and consequently evaluated based on the Oliver and Pharr method [42]. The indentation depths were kept below 10 % of the coating thickness to reduce the substrate interference. The 10 % rule is adequate only for hardness measurement [43]. Furthermore, the residual stresses were calculated based on the Stoney's equation and the curvature measurements done for the coated substrates using an optical profilometry (PS50, Nanovea).

3. Results and discussions

3.1. Phase analysis and microstructure

Fig. 1 shows the cross-sectional SEM images of the as-deposited $CrB_{1.5}$ and alloyed Cr-(Mo)-Si-B_{2-z} coatings with their corresponding chemical compositions. The binary $CrB_{1.5}$ film exhibits a columnar microstructure with extended grains along the growth direction. The addition of Si in the ternary Cr-Si-B_{2-z} coatings results in grain refinement with finer microstructures and relatively smooth surfaces. The Mo-containing Cr-Mo-Si-B_{2-z} coatings show fine-structured dense morphologies which tend to grow featureless by increasing the Mo—Si content. The thickness of the as-deposited coatings ranges between 2 and 2.5 µm for the ternary Cr-Si-B_{2-z}, while the quaternary Cr-Mo-Si-B_{2-z} exhibit thicknesses between 3 and 4.5 µm. The chemical analysis by ToF-ERDA reveals for all coatings sub-stoichiometric boron compositions with B/TM <2, see Table 1. Generally, sputter-deposited CrB_{2-z} films typically exhibit a lower B/Cr ratio compared to the employed target compositions, also well described in the literature with ratios between 1 and 1.5 while using stoichiometric targets [44–46]. Furthermore, the boron content in the alloyed coatings decreases with increasing Si content. In a Cr-Si-B_2 system, the Si tends to occupy both Cr- and B-sites in their corresponding sublattices [20]. However, the system is prone to form Si grain boundary segregates upon reaching a solubility limit of about 4 at. % [20]. For all coatings the oxygen content was below 1.6 at. %.

Fig. 2 depicts the structural analysis by XRD for all Cr-(Mo)-Si-B_{2-z} coatings as well as the binary $CrB_{1.5}$. The Al_2O_3 substrate peaks are marked with gray dotted vertical lines. The binary $CrB_{1.5}$ coating obtains a 001 preferred orientation in its hexagonal AlB_2 structure type (SG 191). The addition of Si in $Cr_{0.38}Si_{0.08}B_{0.54}$ results in a change of the preferred orientation from 001 to 100, while maintaining the single hexagonal structure with no other additional phases. However, a further increase in Si content results in amorphization of the $Cr_{0.37}Si_{0.16}B_{0.47}$ coating with diminished peak intensities. The Si addition results in a slight shift of the low-intensity (001) peak to higher 2θ indicating a decrease in the *c* lattice parameter compared to the binary coating. Furthermore, the quaternary Mo-containing Cr-Mo-Si-B_{2-z} coatings (see

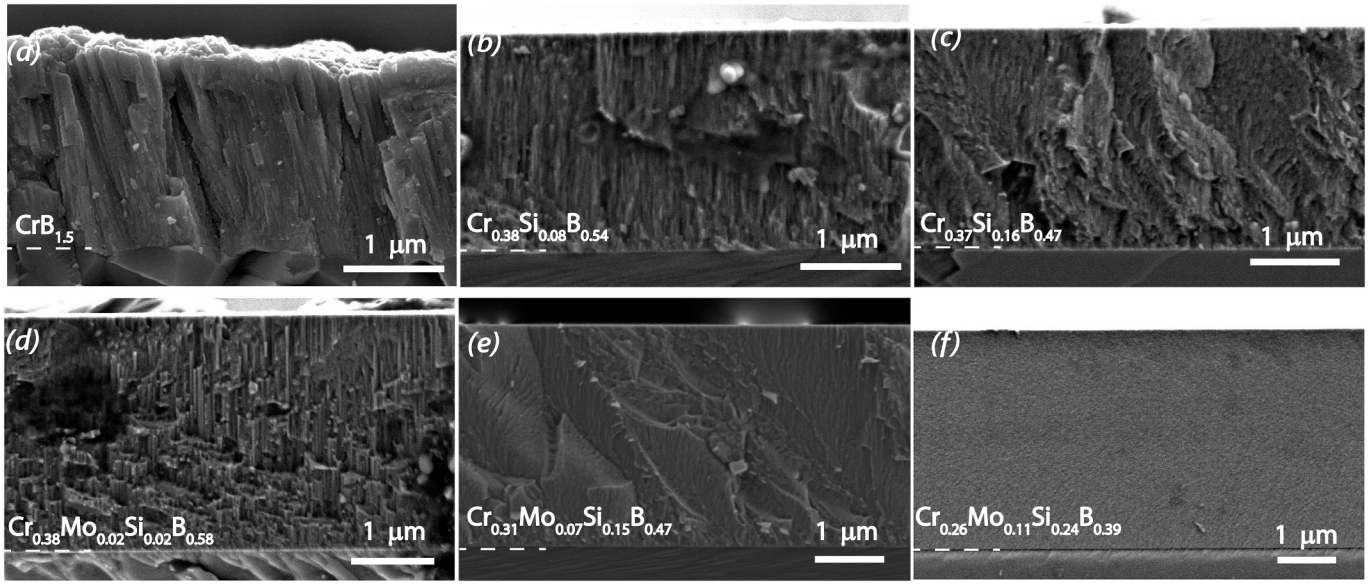

Fig. 1. Cross sectional SEM images of the binary $CrB_{1.5}$ and alloyed Cr-(Mo)-Si-B_{2-z}-based coatings and their corresponding chemical compositions.

Table 1
Chemical composition and mechanical properites (H and E) data of all grown Cr-(Mo)-Si-B_{2-z} coating materials.

Sample	Coating material	Chemical composition [at. %]						H [GPa]	E [GPa]
		Cr	Mo	Si	B	O	B/(Cr + TM)		
1	$CrB_{1.5}$	40	–	–	59.1	0.9	1.48	25.1 ± 1.5	414 ± 37
2	$Cr_{0.38}Si_{0.08}B_{0.54}$	37.8	–	7.4	53.2	1.6	1.42	22.1 ± 1.5	392 ± 26
3	$Cr_{0.33}Si_{0.08}B_{0.59}$	33.4	–	7.4	59.2	–	1.77	20.1 ± 0.9	306 ± 14
4	$Cr_{0.31}Si_{0.13}B_{0.56}$	30.6	–	13.6	55.8	–	1.77	20.3 ± 0.8	355 ± 10
5	$Cr_{0.30}Si_{0.14}B_{0.56}$	30.4	–	13.6	56	–	1.84	20.4 ± 0.9	338 ± 13
6	$Cr_{0.37}Si_{0.16}B_{0.47}$	36.2	–	16.2	46.2	1.5	1.27	21.1 ± 0.8	356 ± 19
7	$Cr_{0.38}Mo_{0.02}Si_{0.02}B_{0.58}$	37.5	2.5	1.8	57	1.2	1.45	26 ± 1.5	386 ± 27
8	$Cr_{0.33}Mo_{0.07}Si_{0.07}B_{0.53}$	32.2	6.8	6.9	52.9	0.4	1.32	25.9 ± 1.5	403 ± 21
9	$Cr_{0.32}Mo_{0.06}Si_{0.11}B_{0.51}$	31.9	6.2	10.6	50.2	0.3	1.34	24.1 ± 1.4	377 ± 19
10	$Cr_{0.31}Mo_{0.07}Si_{0.14}B_{0.48}$	31	6.4	13.4	47.8	0.5	1.26	21.5 ± 1.2	367 ± 18
11	$Cr_{0.31}Mo_{0.07}Si_{0.15}B_{0.47}$	30.4	6.9	15.3	46.3	1.1	1.27	21.2 ± 1.1	365 ± 23
12	$Cr_{0.26}Mo_{0.11}Si_{0.24}B_{0.39}$	25.4	10.6	24.1	38.9	1.0	1.05	20.4 ± 0.9	324 ± 13

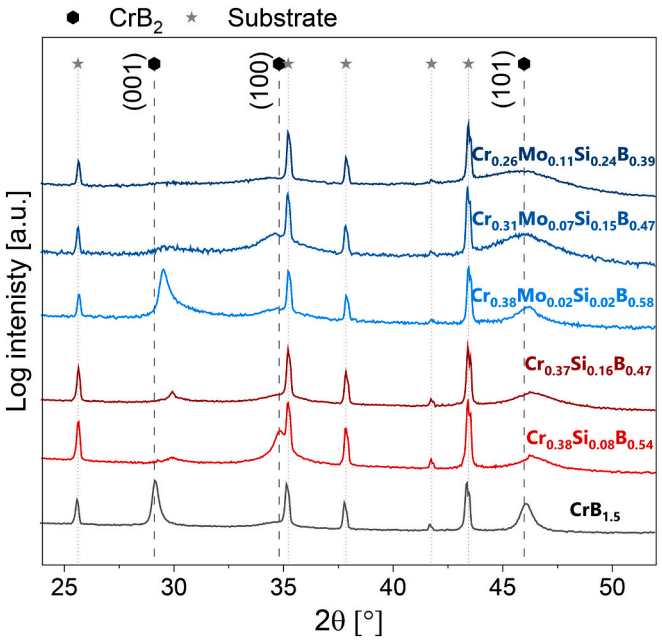

Fig. 2. X-ray diffractograms of all the CrB_2-based coatings deposited on polycrystalline Al_2O_3 substrates at −40 V substrate bias potential.

blue XRD patterns within Fig. 2) exhibit only peaks of the single hexagonal phase. For the low-alloyed $Cr_{0.38}Mo_{0.02}Si_{0.02}B_{0.58}$ coating, a preferred 001 orientation can be observed. However, the peaks diminished by increasing the Mo—Si content within the coatings obtaining clear indications of grain refinement for $Cr_{0.31}Mo_{0.07}Si_{0.15}B_{0.47}$ (as also depicted in Fig. 1). Even higher Mo—Si contents lead to an X-ray amorphous character, see $Cr_{0.26}Mo_{0.11}Si_{0.24}B_{0.39}$ in Fig. 2. The incorporation of Si is reported to typically segregate along grain boundary regions causing grain/columnar refinement and resulting in the formation of amorphous structures at high alloying contents [47,48].

3.2. Mechanical properties

Fig. 3 presents (a) the hardness values of all as-deposited coatings as a function of the Si content as well as (b) the applied substrate bias potential during film growth. The highest hardness values were obtained for the low alloyed Mo-containing $Cr_{0.38}Mo_{0.02}Si_{0.02}B_{0.58}$ followed by the binary $CrB_{1.5}$, both predominantly exhibiting a preferred 001 orientation in the single-phase hexagonal structure (see Fig. 3). Moreover, the other alloyed coatings show a decrease in hardness by increasing Si content (see Fig. 3a), where the lowest hardness value of 20.3 ± 0.9 is recorded for $Cr_{0.26}Mo_{0.11}Si_{0.24}B_{0.39}$ exhibiting an amorphous character (as proven by XRD analysis, see Fig. 2). Nevertheless, the applied substrate bias potential shows a clear influence especially on the hardness of the Mo-containing Cr-Mo-Si-B_{2-z} coatings, wherein the hardness increased from 21.1 ± 1.1 GPa to 25.8 ± 1.4 GPa as the bias rises from −40 V to −150 V (Fig. 3b). This increase in hardness is related

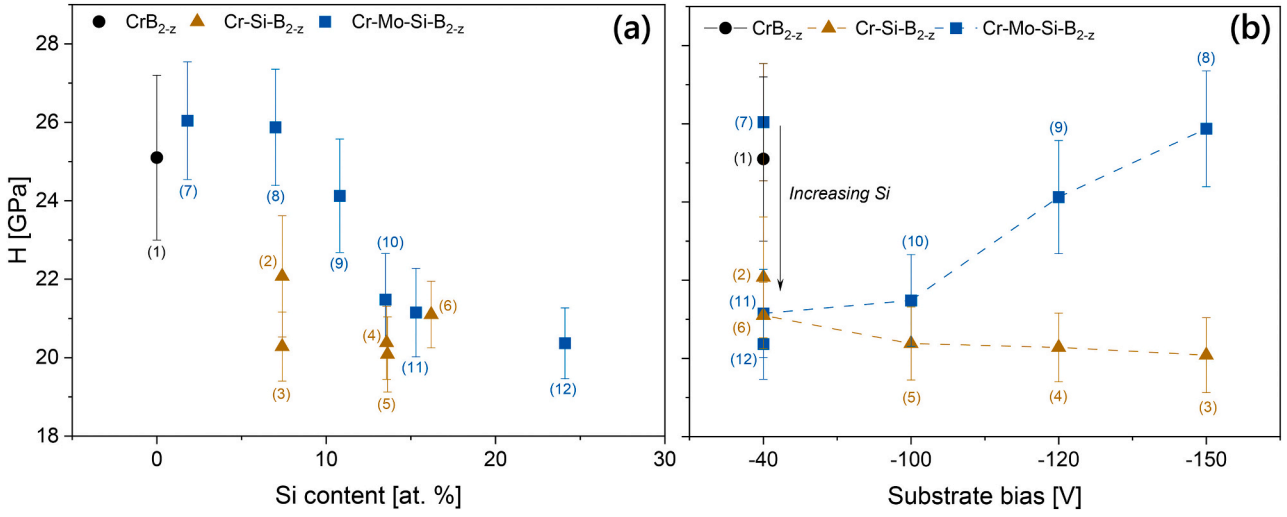

Fig. 3. Hardness of all as-deposited CrB_2-based coatings as a function of (a) Si content (b) substrate bias potential. The coatings in (a) are deposited at a substrate bias potential of −40 V. The indicated sample numbers correspond to the detailed chemical composition of the coatings included in Table 1.

to the enhanced degree of crystallinity and the reduced Si content within the coatings at higher bias potentials (see Fig. 4). The increase in bias potential is accompanied by increased Ar ion irradiation during film growth, hence enhancing adatom mobility as well as preferential re-sputtering of the weakly bonded Si (as observed by the decreased Si content at higher bias potential). This effect beneficially promotes the formation of a single solid solution phase within the Mo-containing Cr-Mo-Si-B_{2-z} coatings indicated by the pronounced hexagonal peaks during structural analysis (see Fig. 4). The measured residual stresses within the coatings did not show a significant change with the varied bias potential, where the values stayed in the range of −0.2 and − 0.4 GPa for the quaternary Cr-Mo-Si-B_{2-z} coatings (see Fig. S1 in the Appendix). For the ternary Cr-Si-B_{2-z} coatings, the increased bias potential kept the hardness more or less unchanged, suggesting no strong influence on the Si distribution within the growing film. In general, Si alloying in transition metal diborides is expected to reduce hardness as reported previously in [15,19,20]. Nevertheless, in case of the Mo-containing coatings, the high bias promoted the formation of single phased solid solutions of (Cr,Mo)B_2 resulting in high hardness values up to ~26 GPa – even though the 001 orientation is not predominant.

3.3. Oxidation behavior

To study the oxidation behavior of the Cr-(Mo)-Si-B_{2-z} coatings, dynamic oxidation measurements have been performed on coated polycrystalline Al_2O_3 substrates in a TG system at a heating rate of 10 °C/min up to 1400 °C in synthetic air. Fig. 5 summarizes the mass gain (in percentage of the actual coating mass) during dynamic oxidation of all alloyed Cr-(Mo)-Si-B_{2-z} coatings as a function of the annealing temperature. The mass signal for the binary $CrB_{1.5}$ coating is added for comparison and indicated by a black dashed line. The binary $CrB_{1.5}$ exhibits an onset oxidation temperature of 600 °C, proven by a previously constant mass signal indicating no pronounced oxidation process below this temperature. The mass signal starts to increase sharply above 600 °C in a step-wise behavior until 1100 °C indicating the complete oxidation of the coating material followed by a mass loss due to the formation of volatile oxides such as CrO_3 [49,50] and B_2O_3 [51]. The addition of Si clearly improves the oxidation resistance (as shown in Fig. 5a), where the slopes of the ternary coatings significantly reduce upon alloying compared to the binary $CrB_{1.5}$. The high Si-containing $Cr_{0.37}Si_{0.16}B_{0.47}$ exhibits nearly constant mass signal up to 1200 °C followed by a slight increase, indicating the formation of a highly protective Si-based scale. Moreover, the quaternary alloyed Cr-Mo-Si-B_{2-z} coatings exhibit outstanding high-temperature oxidation resistance, clearly outperforming the ternary counterparts (see Fig. 5b). The mass curve completely flattens for both $Cr_{0.31}Mo_{0.07}Si_{0.15}B_{0.47}$ and $Cr_{0.26}Mo_{0.11}Si_{0.24}B_{0.39}$ with no mass gains or losses up to 1300 °C. This is clearly related to the formation of protective scales inhibiting the oxygen inward diffusion.

To further investigate the detailed oxidation mechanisms and especially the oxide scale formation of the ternary and quaternary coatings, we selected two representative coatings with similar Si content for more detailed analysis. Therefore, $Cr_{0.37}Si_{0.16}B_{0.47}$ and $Cr_{0.31}Mo_{0.07}Si_{0.15}B_{0.47}$ have been oxidized at 1200 °C in ambient air and subsequently analyzed concerning their phase formation and changes in the morphology.

In Fig. 6, the TEM analysis for the oxidized $Cr_{0.37}Si_{0.16}B_{0.47}$ coating after 1 h at 1200 °C in ambient air is presented. The high-angle annular dark-field (HAADF) image of the coating cross-section shows a globular morphology being a clear indication for recrystallization due to reaching temperatures above 0.5•T_M (melting temperature). In addition, a high degree of porosity is visible in Fig. 6a. Based on the mass contrast, the HAADF image also indicates phase separations at this temperature, see the bright and dark regions. The corresponding EELS linescan (see Fig. 6e) proves the bright regions to be Cr- and B-rich, whereas the dark regions are enriched in Si. The phase separation of Si from the CrB_{2-z} matrix is in good agreement with the solubility limit of around 4 at. % suggested in [20]. At this high temperature (1200 °C), the segregated Si has high mobility and tends to diffuse towards the surface leaving voids within the coating, see Fig. 6a. On the very top, a thin double-layered oxide is formed with a convoluted surface structure. The elemental EDX maps of the surface near regions (see Fig. 6d) reveal the outer layer to be a Cr-based oxide with a thickness of around 200 nm, while the

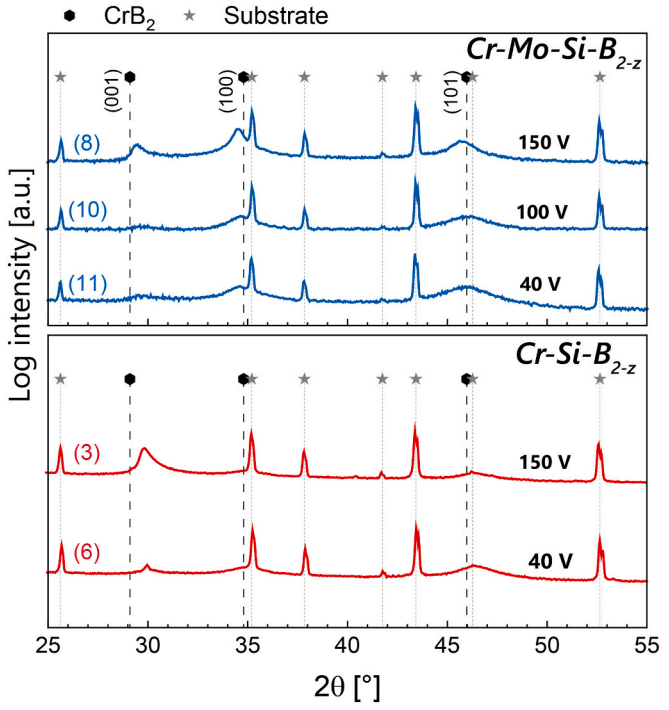

Fig. 4. X-ray diffractograms of (a) Cr-Si-B_{2-z} and (b) Cr-Mo-Si-B_{2-z} coatings deposited at different substrate bias potential. The indicated sample numbers correspond to the detailed chemical composition of the coatings included in Table 1.

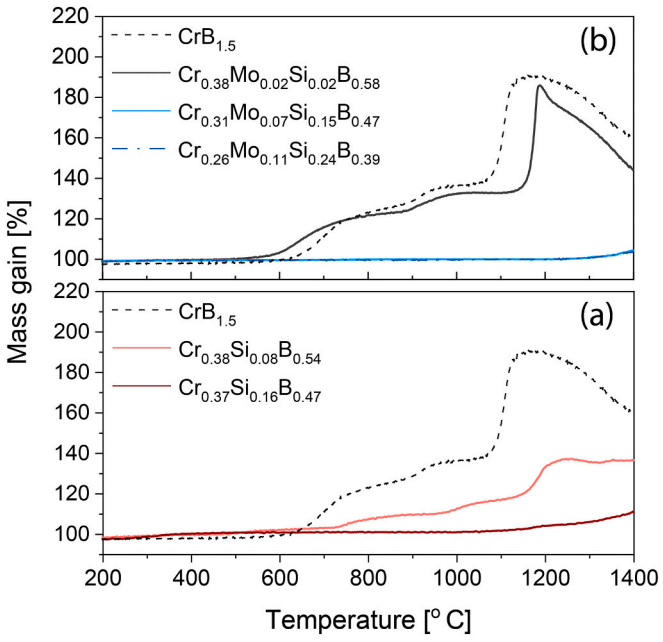

Fig. 5. TG curves of coating mass change during dynamic oxidation of (a) ternary Cr-Si-B_{2-z} and (b) quaternary Cr-Mo-Si-B_{2-z} coatings in synthetic air using a heating rate of 10 °C/min. The mass signal of binary $CrB_{1.5}$ coating is added and indicated by a dashed black line in (a) and (b).

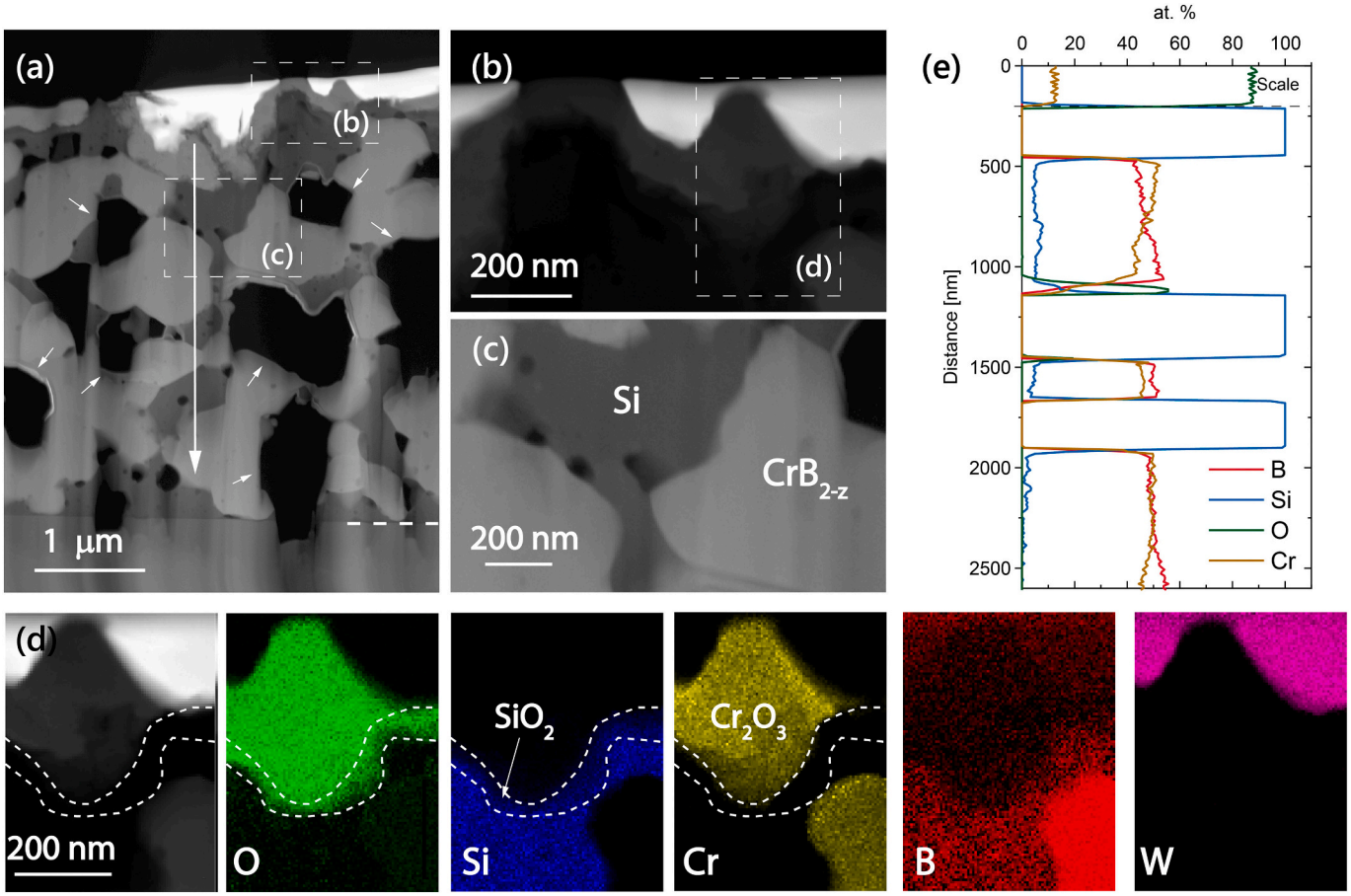

Fig. 6. TEM analysis of $Cr_{0.37}Si_{0.16}B_{0.47}$ coating oxidized in ambient air at 1200 °C for 1 h. (a) High-angle annular dark-field (HAADF) image of the coating cross section with the substrate at the bottom and scale on the top. (b) Magnified area of top oxide scale. (c) Magnified area indicated in (a). (d) EDX elemental maps of the area illustrated in (b). (e) EELS linescan over the coating cross section as indicated in by a white line in (a).

inner oxide layer is a thin Si-based scale of only 50 nm. The formation of this Si—O layer at the scale-coating interface is the key to the high-temperature oxidation resistance (see Fig. 5), as it acts as an efficient barrier against oxygen inward diffusion. This barrier also slows down the outward diffusion of Cr, which typically has the tendency to form volatile oxides in these temperature regimes [52,53]. It must be noted that the EDX analysis is not accurate regarding the quantification of light elements which results in an overestimation of the B content in the elemental map.

Fig. 7 presents the TEM analysis of the oxidized $Cr_{0.31}Mo_{0.07}Si_{0.15}B_{0.47}$ coating at 1200 °C for 1 h. The cross-sectional HAADF image shows that the unaffected coating is recrystallized and exhibits a globular morphology with relatively large grains. The different phases can be identified based on their mass contrast where brighter grains indicate elements with high atomic number. This coating forms a separate phase of $MoSi_2$ in addition to the main phase of hexagonal solid solution $CrMoB_{2-z}$ (see also the structural analysis in Fig. 8). The formed oxide scale on top is composed of two layers: an outer crystalline layer of Cr_2O_3 and an inner thin layer of amorphous SiO_2. Additionally, the observed bright grains at the scale-coating interface are rich in Mo and B. The formation of a Si-depleted MoB_x phase at the scale near region can be related to the outward diffusion of Cr and Si to form the corresponding top oxide scales. Moreover, a small Si region which is depleted in oxygen is observed right beneath the scale. Compared to the ternary coating, the $Cr_{0.31}Mo_{0.07}Si_{0.15}B_{0.47}$ exhibits higher stability and a lower degree of porosity and voids at the same temperature regime. This positive effect is attributed to the presence of Mo which tends to form locking phases with both Si and B ($MoSi_2$ and MoB_x), and hence, retarding the mobility of the available Si within the microstructure. The formation of $MoSi_2$ and MoB_x is in good agreement with previously reported bulk $ZrB_2/MoSi_2$ [23,28] also obtaining beneficial influence on the high-temperature oxidation resistance. The $MoSi_2$ phase contributes to the formation of SiO_2 as an oxidation product, while suppressing the formation of detrimental volatile B_2O_3 by forming a MoB secondary phase [23].

To further describe the phase evolution during annealing, in-situ XRD analysis of powdered $Cr_{0.31}Mo_{0.07}Si_{0.15}B_{0.47}$ coatings have been conducted in vacuum. As depicted in Fig. 8, the $Cr_{0.31}Mo_{0.07}Si_{0.15}B_{0.47}$ coating exhibits a single phased (AlB_2-structure) solid solution up to ~550 °C. A subtle hump can be observed at 600 °C between 40 and 42° indicating the initiation of phase decomposition and formation of tetragonal $MoSi_2$ phase. By increasing the temperature, the $MoSi_2$ peaks become pronounced, while the intensity of the main peaks of the AlB_2-structure significantly increases due to the recrystallization effect at elevated temperatures as described previously in the TEM analysis (see Fig. 7).

The high-temperature phase evolution in $Cr_{0.31}Mo_{0.07}Si_{0.15}B_{0.47}$ is corroborated by APT analysis with local chemical compositions at the nanometer scale. The reconstructions of atomic positions and concentration profiles for $Cr_{0.31}Mo_{0.07}Si_{0.15}B_{0.47}$ in the as-deposited state and after annealing at 800 °C are shown in Fig. 9. As-deposited $Cr_{0.31}Mo_{0.07}Si_{0.15}B_{0.47}$ exhibits a homogenous composition with random elemental distribution for Cr, B and Mo in the entire volume (see Fig. 9a and b). Nevertheless, chemical modulations in the nm-scale can be observed for Si which shows variation between 8 and 14 at. % (see Fig. 9b), indicating the tendency for clustering in specific regions within

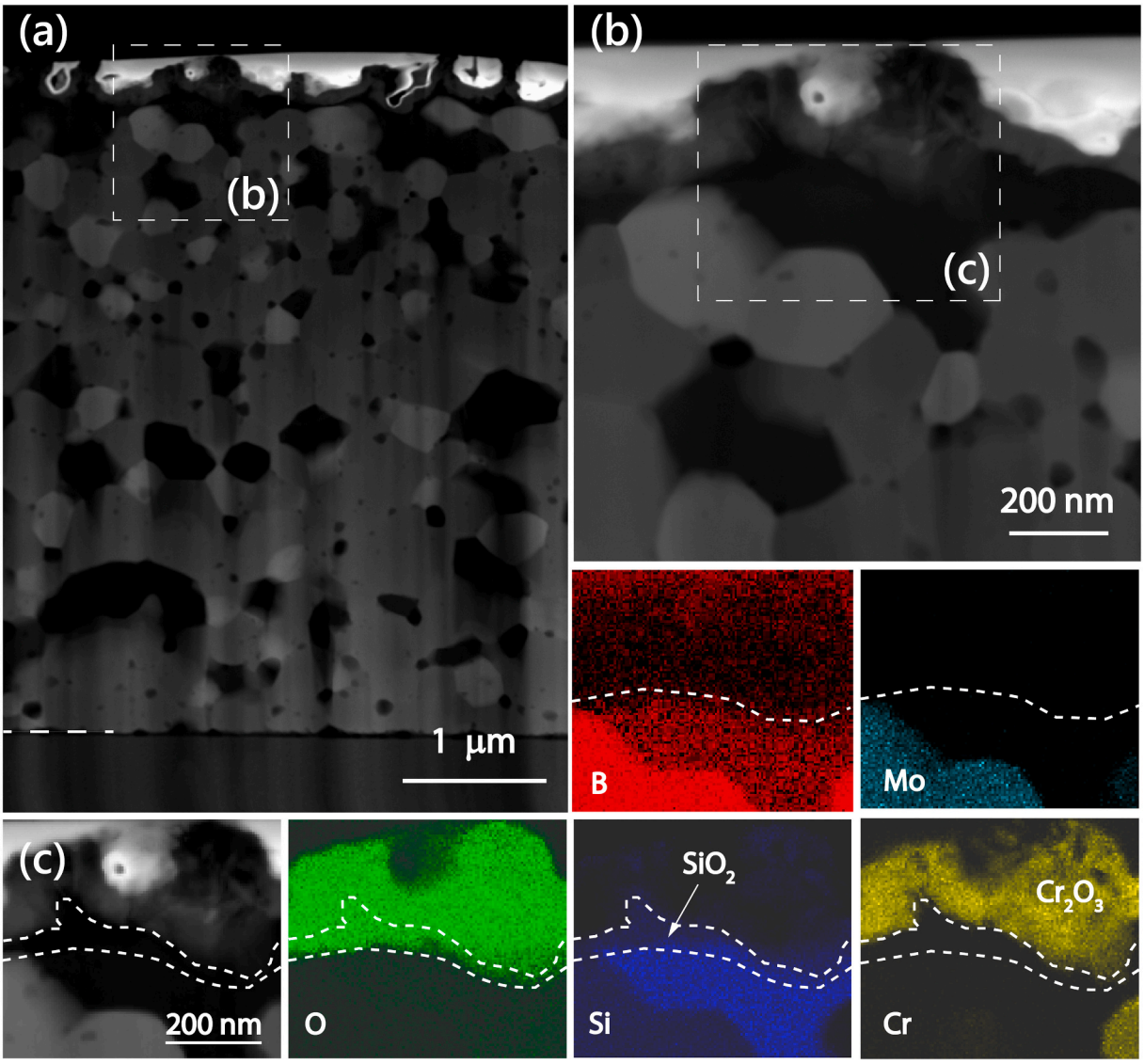

Fig. 7. TEM analysis of $Cr_{0.31}Mo_{0.07}Si_{0.15}B_{0.47}$ coating oxidized in ambient air at 1200 °C for 1 h. (a) High-angle annular dark-field (HAADF) image of the coating cross section with the substrate at the bottom and scale on the top. (b) Magnified area of top oxide scale. (c) EDX elemental maps of the area illustrated in (b).

the microstructure (e.g. at grain boundaries). At 800 °C, the Si clustering is significantly pronounced, as segregations enriched with Si and Mo can be seen in Fig. 9c. Cr and B are depleted within the segregated regions, while the concentrations of Si and Mo within the segregations reach up to 48 and 22 at. %, respectively (see Fig. 9d). It can be inferred that these segregated regions are $MoSi_2$ domains based on the previously discussed XRD (Fig. 8). However, the Mo concentration in the matrix remains around 5 at. %, suggesting the dissolution of Mo in the hexagonal (Cr, Mo)B_{2-z} phase upon annealing without being fully consumed during the $MoSi_2$ formation.

To investigate the long-term stability of the $Cr_{0.31}Mo_{0.07}Si_{0.15}B_{0.47}$ coating, we performed isothermal annealing in ambient air at 1200 °C up to 30 h. Fig. 10 shows the cross-sectional SEM images at different time periods. These cross-sections have been prepared by FIB milling. The white dashed lines indicate both the coating-scale and substrate-coating interfaces, while the blue dashed line indicates the interface between the oxide scale and the FIB deposited protective layer. After 3 h, the $Cr_{0.31}Mo_{0.07}Si_{0.15}B_{0.47}$ coating forms a top oxide scale of ~900 nm with an amorphous character accompanied by a thin crystalline Cr-based oxide (similar to the one obtained after 1 h). The scale thickness increases after 10 h to around 2.4 µm. After 30 h, the oxide scale is more uniform and the thickness stays at about 2.5 µm with negligible increase compared to the thickness obtained after 10 h, demonstrating the strongly retarded oxidation kinetics. The formed scale is dense and mainly amorphous, with a top bright appearing nanocrystalline oxide layer (highlighted by small arrows in Fig. 10). The underlying coating is intact with some porosities.

Fig. 11 shows a more detailed analysis (cross section and EDX line scan) of the $Cr_{0.31}Mo_{0.07}Si_{0.15}B_{0.47}$ oxidized coating after 10 h. The formed oxide scale is Si-rich with small amounts of Cr confirming the layered structure of crystalline Cr_2O_3 on top of an amorphous SiO_2. Beneath this scale, a region depleted in Cr and enriched in both Si and Mo is recognizable, indicating the formation of $MoSi_2$. Moreover, a Si-depleted zone can be observed at the substrate near region. The coating is still maintaining the hexagonal CrB_2 in addition to the $MoSi_2$ phase as confirmed by XRD analysis (see Fig. S3, in Appendix). The outstanding oxidation resistance after 30 h at 1200 °C is attributed to the beneficial phase formation of $MoSi_2$ acting as a locking phase for the highly mobile Si, and reservoir for the SiO_2 formation.

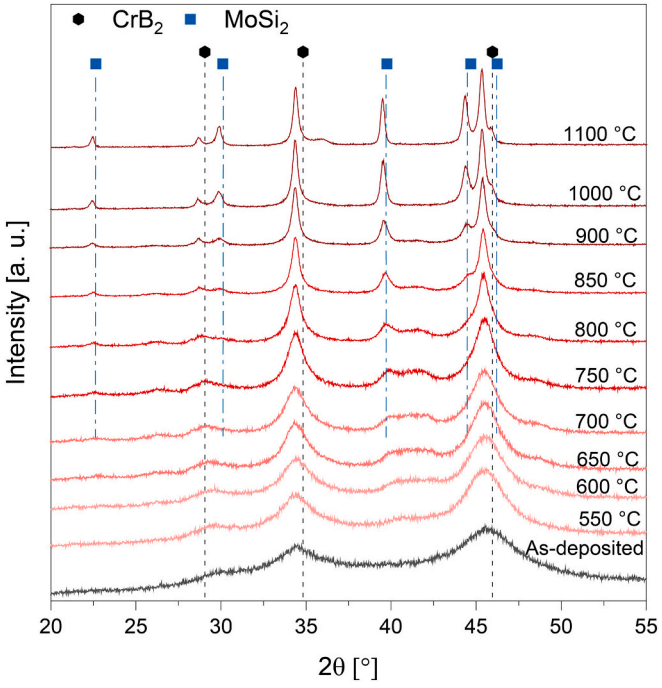

Fig. 8. In-situ X-ray diffraction analysis of vacuum annealed powder sample of $Cr_{0.31}Mo_{0.07}Si_{0.15}B_{0.47}$ coating up to 1100 °C.

4. Conclusions

In this study, we investigated the influence of $TMSi_2$ alloying on the oxidation behavior of CrB_{2-z}-based coatings. Ternary and quaternary Cr-(Mo)-Si-B_{2-z} films have been deposited by DC magnetron sputtering from alloyed $CrB_2/TMSi_2$ targets (TM = Cr or Mo). All Cr-(Mo)-Si-B_{2-z} coatings exhibit hexagonal single-phase AlB_2-type structures, except $Cr_{0.26}Mo_{0.11}Si_{0.24}B_{0.39}$ where the high Si content leads to a nanocrystalline/X-ray amorphous morphology. Moreover, the Si-alloying in the ternary Cr-Si-B_{2-z} coatings decreases the hardness (~22GPa) compared to the binary $CrB_{1.5}$ (~25 GPa). In contrast, the Mo-containing Cr-Mo-Si-B_{2-z} exhibited relatively high hardness values up to 26 GPa due to the formation of (Cr,Mo)B_2 solid solutions. Increased bias potentials promoted the formation of single-phase Cr-Mo-Si-B_{2-z} coatings with enhanced crystallinity and mechanical properties. Furthermore, the oxidation behavior of the alloyed coatings has been examined up to 1400 °C. The addition of Si drastically improves the high-temperature oxidation resistance of the ternary and quaternary alloyed Cr-(Mo)-Si-B_{2-z} coatings. The $Cr_{0.37}Si_{0.16}B_{0.47}$ coating exhibits high oxidation resistance with negligible mass gain up to 1200 °C, owing to the formation of highly protective SiO_2 scales with Cr_2O_3 layers on top. After 1 h at 1200 °C, $Cr_{0.37}Si_{0.16}B_{0.47}$ decomposed into a predominant diboride phase next to elemental Si which tends to diffuse towards the surface. This, in a further consequence, promotes the formation of voids and leaves a high porosity within the unoxidized microstructure. In contrast, the quaternary $Cr_{0.31}Mo_{0.07}Si_{0.15}B_{0.47}$ coating revealed a superior oxidation resistance with lower porosity compared to the ternary $Cr_{0.37}Si_{0.16}B_{0.47}$ at 1200 °C. The enhanced oxidation resistance is

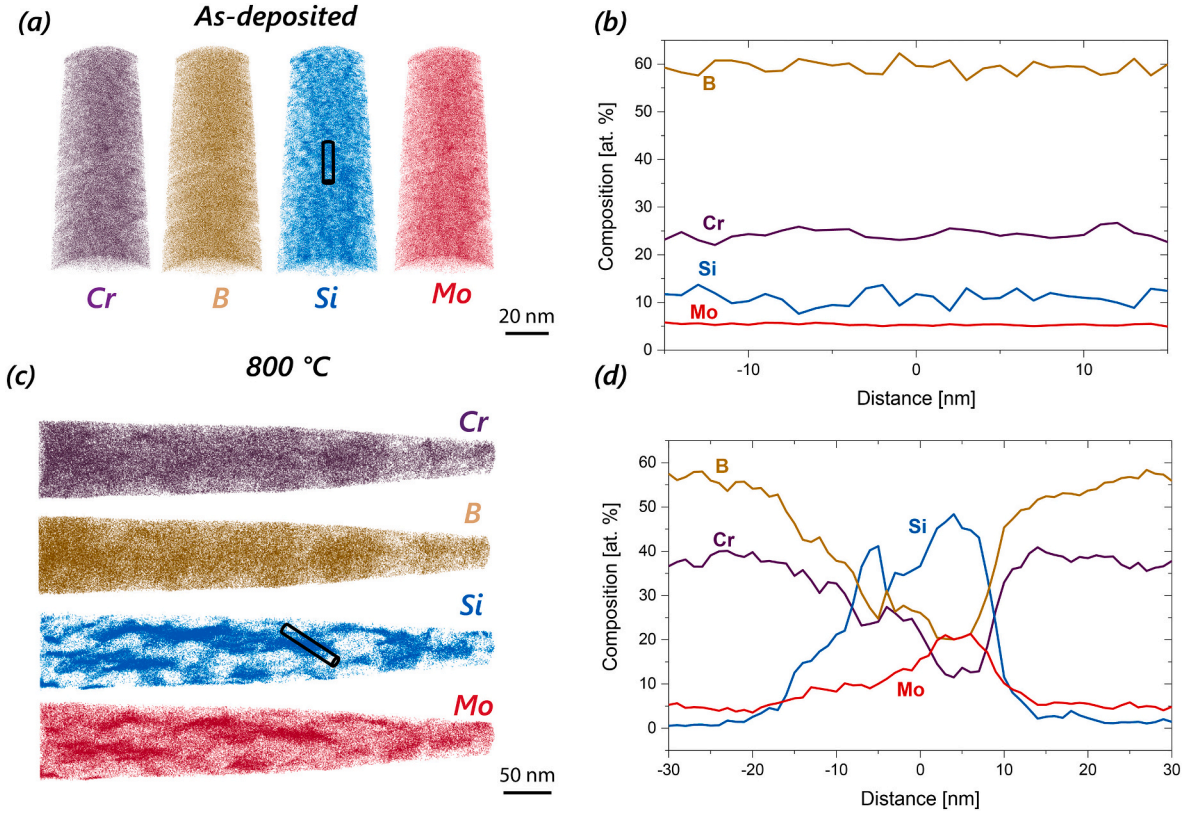

Fig. 9. APT characterization of $Cr_{0.31}Mo_{0.07}Si_{0.15}B_{0.47}$ in the as-deposited and annealed states. (a) Reconstructions of Cr, B, Si and Mo for the as-deposited $Cr_{0.31}Mo_{0.07}Si_{0.15}B_{0.47}$, and (b) concentration profile of the cylindrical region indicated in (a). (c) Reconstructions of Cr, B, Si and Mo for the annealed $Cr_{0.31}Mo_{0.07}Si_{0.15}B_{0.47}$ at 800 °C, and (d) concentration profile of the cylindrical region indicated in (c).

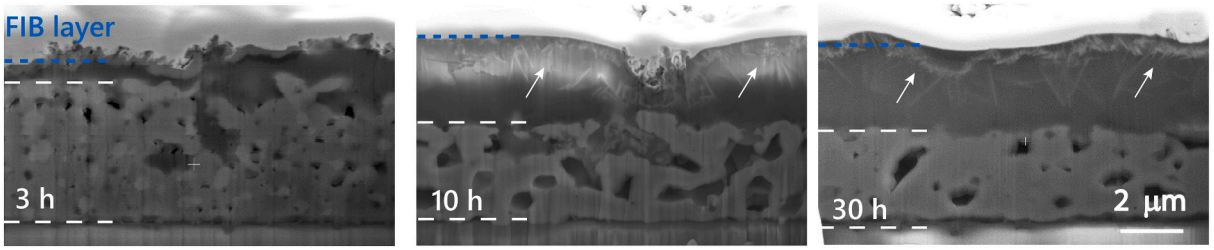

Fig. 10. Cross-sectional SEM images of $Cr_{0.31}Mo_{0.07}Si_{0.15}B_{0.47}$ oxidized coatings at 1200 °C in ambient air at different annealing times. The blue dotted line indicates the interface between the FIB deposited layer and oxide scale, while the white dashed lines indicate the substrate-coating and coating-scale interfaces. (For interpretation of the references to colour in this figure legend, the reader is referred to the web version of this article.)

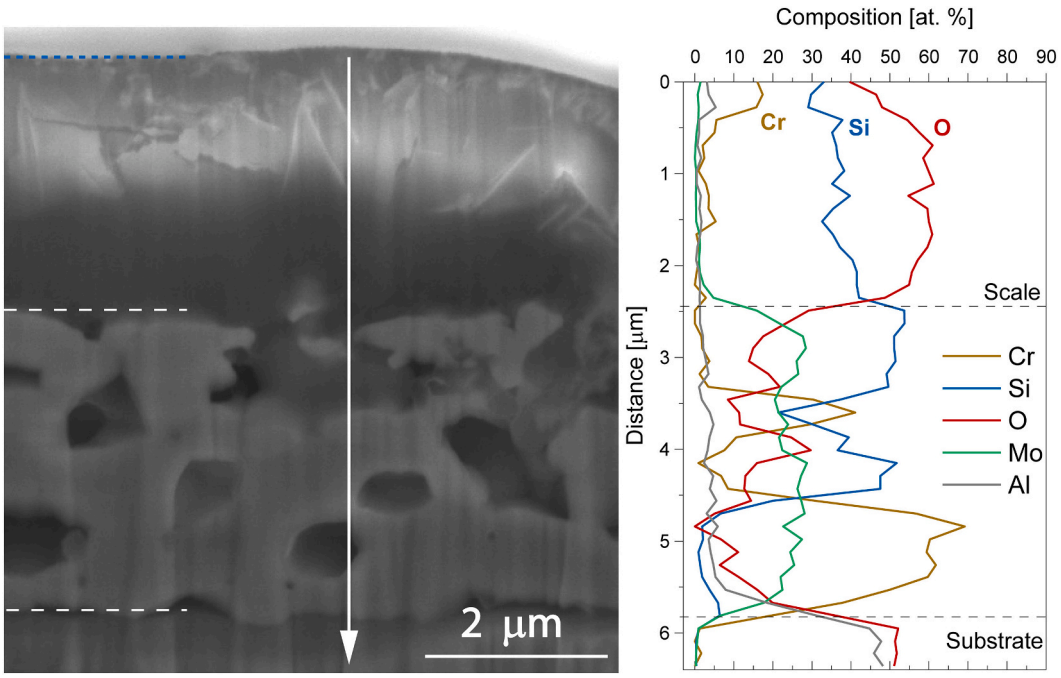

Fig. 11. SEM cross-sectional image of $Cr_{0.31}Mo_{0.07}Si_{0.15}B_{0.47}$ coating oxidized at 1200 °C for 10 h with EDX linescan analysis on the right-hand side. The position of the linescan is indicated by the white line in the SEM image.

attributed to the available Mo and the formation of $MoSi_2$ instead of elemental Si (as revealed by APT analysis). Mo controls the outward diffusion and mobility of Si by forming the $MoSi_2$ phase, which contributes to the formation of the highly protective SiO_2 as an oxidation product while suppressing the formation of the detrimental volatile B_2O_3 by forming a MoB_x secondary phase at the scale interface. The quaternary $Cr_{0.31}Mo_{0.07}Si_{0.15}B_{0.47}$ coating maintained an outstanding oxidation resistance up to 30 h at 1200 °C by forming a dense amorphous Si-based oxide scale with a thin Cr_2O_3 on top.

In summary, this study demonstrates the high potential of quaternary Cr-Mo-Si-B_{2-z} as promising coating materials for high-temperature applications, owing to their superior oxidation resistance compared to their binary and ternary counterparts.

CRediT authorship contribution statement

A. Bahr: Conceptualization, Investigation, Writing – original draft. **T. Glechner:** Investigation. **A. Grimmer:** Investigation. **T. Wojcik:** Investigation. **R. Hahn:** Investigation. **P. Kutrowatz:** Investigation. **M. Podsednik:** Investigation. **A. Limbeck:** Resources. **M. Heller:** Investigation. **J. Ramm:** Resources, Writing – review & editing. **O. Hunold:** Resources. **S. Kolozsvári:** Resources. **P. Polcik:** Resources. **E. Ntemou:** Investigation, Writing – review & editing. **D. Primetzhofer:** Resources, Writing – review & editing. **P. Felfer:** Resources. **H. Riedl:** Supervision, Project administration, Writing – review & editing.

Declaration of competing interest

The authors declare that they have no known competing financial interests or personal relationships that could have appeared to influence the work reported in this paper.

Data availability

Data will be made available on request.

Acknowledgments

The financial support by the Austrian Federal Ministry for Digital and Economic Affairs, the National Foundation for Research, Technology and Development and the Christian Doppler Research Association is gratefully acknowledged (Christian Doppler Laboratory “Surface Engineering of high-performance Components”). We also thank for the financial support of Plansee SE, Plansee Composite Materials GmbH, and Oerlikon Balzers, Oerlikon Surface Solutions AG. We also thank the X-ray center (XRC) of TU Wien for beam time as well as the electron

microscopy center - USTEM TU Wien - for using the SEM and TEM facilities. Finally, we acknowledge TU Wien Bibliothek for financial support through its Open Access Funding Programme. In addition, the authors thank the RADIATE project for funding our beamtime at the Tandem Laboratory at Uppsala University. Accelerator operation at Uppsala University was supported by the Swedish Research Council VR-RFI (#2019-00191).

Appendix A. Supplementary data

Supplementary data to this article can be found online at https://doi.org/10.1016/j.surfcoat.2023.129733.

References

[1] J.H. Perepezko, The hotter the engine, the better, Science 326 (2009) 1068–1069.
[2] C. Mitterer, Borides in thin film technology, J. Solid State Chem. 133 (1997) 279–291.
[3] W.G. Fahrenholtz, G.E. Hilmas, Ultra-high temperature ceramics: materials for extreme environments, Scr. Mater. 129 (2017) 94–99.
[4] M. Magnuson, L. Hultman, H. Högberg, Review of transition-metal diboride thin films, Vacuum 196 (2022), 110567.
[5] W.G. Fahrenholtz, G.E. Hilmas, Oxidation of ultra-high temperature transition metal diboride ceramics, Int. Mater. Rev. 57 (2012) 61–72.
[6] T.A. Parthasarathy, R.A. Rapp, M. Opeka, R.J. Kerans, A model for the oxidation of ZrB2, HfB2 and TiB2, Acta Mater. 55 (2007) 5999–6010.
[7] J. Thörnberg, B. Bakhit, J. Palisaitis, N. Hellgren, L. Hultman, G. Greczynski, P.O. Å. Persson, I. Petrov, J. Rosen, Improved oxidation properties from a reduced B content in sputter-deposited TiBx thin films, Surf. Coat. Technol. 420 (2021), 127353.
[8] B. Bakhit, J. Palisaitis, J. Thörnberg, J. Rosen, P.O.Å. Persson, L. Hultman, I. Petrov, J.E. Greene, G. Greczynski, Improving the high-temperature oxidation resistance of TiB2 thin films by alloying with Al, Acta Mater. 196 (2020) 677–689.
[9] V. Moraes, H. Riedl, C. Fuger, P. Polcik, H. Bolvardi, D. Holec, P.H. Mayrhofer, Ab initio inspired design of ternary boride thin films, Sci. Rep. 8 (2018) 9288.
[10] C. Fuger, V. Moraes, R. Hahn, H. Bolvardi, P. Polcik, H. Riedl, P.H. Mayrhofer, Influence of tantalum on phase stability and mechanical properties of WB2, MRS Communications 9 (2019) 375–380.
[11] B. Bakhit, D.L.J. Engberg, J. Lu, J. Rosen, H. Högberg, L. Hultman, I. Petrov, J. E. Greene, G. Greczynski, Strategy for simultaneously increasing both hardness and toughness in ZrB2-rich Zr1−xTaxBy thin films, J. Vac. Sci. Technol. A 37 (2019), 031506.
[12] A. Tampieri, A. Bellosi, Oxidation of monolithic TiB2 and of Al2O3-TiB2 composite, J. Mater. Sci. 28 (1993) 649–653.
[13] X. Huang, S. Sun, G. Tu, Investigation of mechanical properties and oxidation resistance of CVD TiB2 ceramic coating on molybdenum, Journal of Materials Research and Technology 9 (2020) 282–290.
[14] S. Dorri, J. Palisaitis, G. Greczynski, I. Petrov, J. Birch, L. Hultman, B. Bakhit, Oxidation kinetics of overstoichiometric TiB2 thin films grown by DC magnetron sputtering, Corros. Sci. 206 (2022), 110493.
[15] T. Glechner, H.G. Oemer, T. Wojcik, M. Weiss, A. Limbeck, J. Ramm, P. Polcik, H. Riedl, Influence of Si on the oxidation behavior of TM-Si-B2±z coatings (TM = Ti, Cr, Hf, Ta, W), Surf. Coat. Technol. 128178 (2022).
[16] C. Fuger, B. Schwartz, T. Wojcik, V. Moraes, M. Weiss, A. Limbeck, C.A. Macauley, O. Hunold, P. Polcik, D. Primetzhofer, P. Felfer, P.H. Mayrhofer, H. Riedl, Influence of ta on the oxidation resistance of WB2−z coatings, J. Alloys Compd. 864 (2021), 158121.
[17] J. Thörnberg, S. Mráz, J. Palisaitis, F.F. Klimashin, P. Ondracka, B. Bakhit, P. Polcik, S. Kolozsvari, L. Hultman, I. Petrov, P.O.Å. Persson, J.M. Schneider, J. Rosen, Oxidation resistance and mechanical properties of sputter-deposited Ti0.9Al0.1B2-y thin films, Surf. Coat. Technol. 442 (2022), 128187.
[18] T. Glechner, A. Bahr, R. Hahn, T. Wojcik, M. Heller, A. Kirnbauer, J. Ramm, S. Kolozsvari, P. Felfer, H. Riedl, High temperature oxidation resistance of physical vapor deposited Hf-Si-B2±z thin films, Corros. Sci. 205 (2022), 110413.
[19] B. Grančič, M. Mikula, T. Roch, P. Zeman, L. Satrapinskyy, M. Gregor, T. Plecenik, E. Dobročka, Z. Hájovská, M. Mičušík, A. Šatka, M. Zahoran, A. Plecenik, P. Kúš, Effect of Si addition on mechanical properties and high temperature oxidation resistance of Ti–B–Si hard coatings, Surf. Coat. Technol. 240 (2014) 48–54.
[20] L. Zauner, A. Steiner, T. Glechner, A. Bahr, B. Ott, R. Hahn, T. Wojcik, O. Hunold, J. Ramm, S. Kolozsvári, P. Polcik, P. Felfer, H. Riedl, Role of Si segregation in the structural, mechanical, and compositional evolution of high-temperature oxidation resistant Cr-Si-B2±z thin films, J. Alloys Compd. 944 (2023), 169203.
[21] T. Glechner, R. Hahn, A. Bahr, T. Wojcik, M. Weiss, J. Ramm, O. Hunold, P. Polcik, H. Riedl, Oxidation resistance of Si doped transition metal diborides at elevated temperatures, Int. J. Refract. Met. Hard Mater. 113 (2023), 106172.
[22] W.G. Fahrenholtz, Thermodynamic analysis of ZrB2–SiC oxidation: formation of a SiC-depleted region, J. Am. Ceram. Soc. 90 (2007) 143–148.
[23] L. Silvestroni, K. Stricker, D. Sciti, H.-J. Kleebe, Understanding the oxidation behavior of a ZrB2–MoSi2 composite at ultra-high temperatures, Acta Mater. 151 (2018) 216–228.
[24] S. Ghadami, E. Taheri-Nassaj, H.R. Baharvandi, F. Ghadami, Effect of in situ SiC and MoSi2 phases on the oxidation behavior of HfB2-based composites, Ceram. Int. 46 (2020) 20299–20305.
[25] D. Sciti, A. Balbo, A. Bellosi, Oxidation behaviour of a pressureless sintered HfB2–MoSi2 composite, J. Eur. Ceram. Soc. 29 (2009) 1809–1815.
[26] D.A. Berztiss, R.R. Cerchiara, E.A. Gulbransen, F.S. Pettit, G.H. Meier, Oxidation of MoSi2 and comparison with other silicide materials, Mater. Sci. Eng. A 155 (1992) 165–181.
[27] A. Bahr, S. Richter, R. Hahn, T. Wojcik, M. Podsednik, A. Limbeck, J. Ramm, O. Hunold, S. Kolozsvári, H. Riedl, Oxidation behaviour and mechanical properties of sputter-deposited TMSi2 coatings (TM = Mo, ta, Nb), J. Alloys Compd. 931 (2023), 167532.
[28] L. Silvestroni, G. Meriggi, D. Sciti, Oxidation behavior of ZrB2 composites doped with various transition metal silicides, Corros. Sci. 83 (2014) 281–291.
[29] S.V. Raj, J. Daniel Whittenberger, B. Zeumer, G. Sauthoff, Elevated temperature deformation of Cr3Si alloyed with Mo, Intermetallics 7 (1999) 743–755.
[30] T.A. Cruse, J.W. Newkirk, Evaluation of methods to produce tough Cr3Si based composites, Mater. Sci. Eng. A 239-240 (1997) 410–418.
[31] A. Bahr, O. Beck, T. Glechner, A. Grimmer, T. Wojcik, P. Kutrowatz, J. Ramm, O. Hunold, S. Kolozsvári, P. Polcik, E. Ntemou, D. Primetzhofer, H. Riedl, Quaternary diborides—improving the oxidation resistance of TiB2 ± z coatings by disilicide alloying, Mater. Res. Lett. 11 (2023) 733–741, https://doi.org/10.1080/21663831.2023.2225554.
[32] P. Ström, D. Primetzhofer, Ion beam tools for nondestructive in-situ and in-operando composition analysis and modification of materials at the tandem Laboratory in Uppsala, J. Instrum. 17 (2022) P04011.
[33] M. Janson, CONTES Instruction Manual, Uppsala University, Uppsala, Sweden, 2004.
[34] M. Mayer, SIMNRA user's guide, (1997).
[35] M. Mayer, Improved physics in SIMNRA 7, Nucl. Instrum. Methods Phys. Res., Sect. B 332 (2014) 176–180.
[36] M.V. Moro, R. Holeňák, L. Zendejas Medina, U. Jansson, D. Primetzhofer, Accurate high-resolution depth profiling of magnetron sputtered transition metal alloy films containing light species: a multi-method approach, Thin Solid Films 686 (2019), 137416.
[37] E. Pitthan, M.V. Moro, S.A. Corrêa, D. Primetzhofer, Assessing boron quantification and depth profiling of different boride materials using ion beams, Surf. Coat. Technol. 417 (2021), 127188.
[38] M. To Baben, M. Hans, D. Primetzhofer, S. Evertz, H. Ruess, J.M. Schneider, Unprecedented thermal stability of inherently metastable titanium aluminum nitride by point defect engineering, Materials Research Letters 5 (2017) 158–169.
[39] A. Cakara, M. Bonta, H. Riedl, P.H. Mayrhofer, A. Limbeck, Development of a multi-variate calibration approach for quantitative analysis of oxidation resistant Mo–Si–B coatings using laser ablation inductively coupled plasma mass spectrometry, Spectrochim. Acta B At. Spectrosc. 120 (2016) 57–62.
[40] H. Riedl, A. Vieweg, A. Limbeck, J. Kalaš, M. Arndt, P. Polcik, H. Euchner, M. Bartosik, P.H. Mayrhofer, Thermal stability and mechanical properties of boron enhanced Mo–Si coatings, Surf. Coat. Technol. 280 (2015) 282–290.
[41] P. Felfer, GitHub - Atom-Probe-Toolbox: Matlab toolbox for APT analysis (https://github.com/peterfelfer/Atom-Probe-Toolbox), (2022).
[42] W.C. Oliver, G.M. Pharr, An improved technique for determining hardness and elastic modulus using load and displacement sensing indentation experiments, J. Mater. Res. 7 (1992) 1564–1583.
[43] S. Zak, C.O.W. Trost, P. Kreiml, M.J. Cordill, Accurate measurement of thin film mechanical properties using nanoindentation, J. Mater. Res. 37 (2022) 1373–1389.
[44] M. Zhou, M. Nose, Y. Makino, K. Nogi, New Cr-B hard coatings by r.f.-plasma assisted magnetron sputtering method, Thin Solid Films, 343–344 (1999) 234–237.
[45] M. Audronis, P.J. Kelly, R.D. Arnell, A.V. Valiulis, Pulsed magnetron sputtering of chromium boride films from loose powder targets, Surf. Coat. Technol. 200 (2006) 4166–4173.
[46] N. Nedfors, D. Primetzhofer, L. Wang, J. Lu, L. Hultman, U. Jansson, Characterization of magnetron sputtered Cr–B and Cr–B–C thin films for electrical contact applications, Surf. Coat. Technol. 266 (2015) 167–176.
[47] M. Zhang, J. Jiang, P. Mareš, J. Houška, J. Vlček, E.I. Meletis, Effect of the Si content on the microstructure of hard, multifunctional Hf–B–Si–C films prepared by pulsed magnetron sputtering, Appl. Surf. Sci. 357 (2015) 1343–1354.
[48] F.V. Kiryukhantsev-Korneev, M.V. Lemesheva, N.V. Shvyndina, E.A. Levashov, A. Y. Potanin, Structure, mechanical properties, and oxidation resistance of ZrB2, ZrSiB, and ZrSiB/SiBC coatings, Protection of Metals and Physical Chemistry of Surfaces 54 (2018) 1147–1156.
[49] A.S. Dorcheh, M.C. Galetz, Challenges in developing oxidation-resistant chromium-based alloys for applications above 900°C, JOM 68 (2016) 2793–2802.
[50] R.T. Grimley, R.P. Burns, M.G. Inghram, Thermodynamics of the vaporization of Cr2O3: dissociation energies of CrO, CrO2, and CrO3, J. Chem. Phys. 34 (1961) 664–667.
[51] M.L. Emiliani, Characterization and oxidation resistance of hot-pressed chromium diboride, Mater. Sci. Eng. A 172 (1993) 111–124.
[52] A. Solimani, T. Nguyen, J. Zhang, D.J. Young, M. Schütze, M.C. Galetz, Morphology of oxide scales formed on chromium-silicon alloys at high temperatures, Corros. Sci. 176 (2020), 109023.
[53] A.S. Ulrich, P. Pfizenmaier, A. Solimani, U. Glatzel, M.C. Galetz, Improving the oxidation resistance of Cr-Si-based alloys by ternary alloying, Corros. Sci. 165 (2020), 108376.